Correlation between plasma characteristics, morphology, and microstructure of sputtered CuAl alloy films with varied target geometry

Materials Research Express

PAPER

Correlation between plasma characteristics, morphology, and microstructure of sputtered CuAl alloy films with varied target geometry

Adie Alwen[1] **and Andrea M Hodge**[1,2,*]

[1] Mork Family Department of Chemical Engineering and Materials Science, University of Southern California, Los Angeles, CA 90089, United States of America

[2] Department of Aerospace and Mechanical Engineering, University of Southern California, Los Angeles, CA 90089, United States of America

[*] Author to whom any correspondence should be addressed.

E-mail: alwen@usc.edu **and** ahodge@usc.edu

OPEN ACCESS

RECEIVED
7 September 2022

REVISED
1 December 2022

ACCEPTED FOR PUBLICATION
13 January 2023

PUBLISHED
25 January 2023

Keywords: morphology, microstructure, magnetron sputtering, target geometry, plasma characterization

Supplementary material for this article is available online

Abstract

The effect of target geometry on coating microstructure and morphology is correlated to changes in deposition conditions, plasma characteristics, and film growth during planar and hollow cathode sputtering. The sputtering plasma properties for the two target geometries were characterized via Langmuir probe analysis as a function of power density and Ar pressure to determine the evolution of ion density for each configuration. Films were then synthesized at the low (0.4 W cm^{-2}) and high (1.2 W cm^{-2}) power densities and characterized using x-ray diffraction, scanning electron microscopy, and electron backscatter diffraction to link changes in texturing, morphology, and microstructure with variations in ion density and sputtering deposition conditions caused by target geometry. It was observed that varying target geometry led to an over threefold increase in deposition rate, homologous temperature, and ion density, which altered the morphology and texture of the film without significant changes to the grain size.

1. Introduction

Magnetron sputtering is a highly tailorable physical vapor deposition (PVD) technique that enables deposition of a vast array of materials, where planar magnetron sputtering is the most commonly used configuration as it allows for unidirectional deposition and high deposition rates [1, 2]. Direct current (DC) magnetron sputtering can effectively deposit conductive materials ranging from single elements to complex alloys, while radio frequency (RF) or reactive sputtering techniques, which utilize high-frequency voltages or flow reactive gases, respectively, are typically used to deposit oxide films, dielectrics, or other non-conductive materials [2–4]. Modified sputtering configurations, including high-power impulse magnetron sputtering (HIPIMS) and ionized physical vapor deposition (I-PVD), have demonstrated the ability to change deposition pathways and film growth mechanisms by ionizing sputtered atoms and increasing overall ion bombardment on the substrate surface during deposition [2, 5–9]. However, studies using non-planar sputtering target geometries to alter film microstructures have been limited. For example, a foundational comparison is still lacking between planar cathode and hollow cathode (also known as inverted cylindrical magnetron (ICM)) sputtering, even though they are two commonly utilized sputtering configurations that provide very distinct angles of incidence during deposition. Understanding the effects of target geometry on plasma characteristics and subsequent film growth presents a novel route to manipulate film morphology and microstructure, which provides access to unexplored microstructures and material properties in sputtered films.

Planar cathodes produce plasma densities that are orders of magnitude lower than HIPIMS and I-PVD, yet, planar sputtering can achieve uniform coatings on surfaces within its line-of-sight by leveraging unidirectional

deposition via techniques such as collimation and long throw sputtering [2, 10, 11]. Qualitative tools for planar film deposition, such as structure zone maps, have been developed to predict changes in grain size, microstructure, and morphology, which enable the technique to tailor deposited film mechanical, optical, thermal, and electronic properties [1, 12–15]. In contrast, due to its target geometry, hollow cathode sputtering is affected by additional factors such as greater plasma densities and a 360° line-of-sight, which in turn affect the microstructure and morphology beyond current structure zone maps representations [1, 12, 15–18]. Typically, ICMs and their plasma discharges have been used in research for off-axis sputtering, where the substrate is outside of the cathode, to coat non-planar and large area substrates ranging from optical lenses to microelectronics [19–24]. To a lesser extent, some studies have investigated ICM sputtering within the cathode volume, analyzing coating wires and adhesion [15, 16, 25–27]. Furthermore, a few studies have explored this target geometry as an alternate deposition configuration for coating substrates with convoluted complex topologies [16, 28, 29].

Recent work on 3D nano- and micro-lattices has demonstrated that coating techniques can increase the material workspace for additively manufactured materials and improve functionality by accessing novel material property spaces [30]. In general, sputter coated nano- and micro-lattices have mostly employed planar target geometries and focused on the coated lattice material properties; some studies have also investigated coating uniformity and observed thickness gradients resulting from the unidirectional deposition of the planar cathode [31–34]. Garcia-Taormina *et al* demonstrated using a hollow cathode that changing target geometry could potentially improve coating coverage on micro-lattice structures by increasing line-of-sight during deposition [28]. Thus, in order to enable further exploration of deposition within complex target geometries, such as the hollow cathode, the correlations between cathode geometry and film growth warrant further research.

In this study, a comprehensive comparison between planar and hollow cathode sputtering using Cu-Al targets, focusing on the influence of target geometry on plasma characteristics, deposition conditions, and film microstructure is presented. Plasma conditions were characterized using a Langmuir Probe at applied power densities ranging from 0.4 to 1.2 W cm^{-2} and Argon pressures ranging from 3 to 30 mTorr. Coatings were then synthesized at the high and low power densities to highlight the effects of changing ion density, deposition rate, and homologous temperature on the film microstructure and morphology. The films were subsequently characterized via x-ray diffraction (XRD), scanning electron microscopy (SEM), and electron backscatter diffraction (EBSD) to observe variations in texture, feature size, and cross-sectional microstructure. Ultimately, this work links target geometry as a variable to change the plasma characteristics, demonstrating a novel route to manipulate and expand coating morphology and microstructure.

2. Methods

Films were deposited on (100) 25 mm × 25 mm Si substrates in a vacuum chamber via DC hollow and planar cathode sputtering using 99.99% Cu-2wt.%Al targets. The target composition was selected since sputtering with Cu and Cu-Al alloys is well documented under planar conditions and these material systems can be easily machined for the hollow cathode geometry [1, 16, 35]. The hollow cathode target (Kurt J Lesker Company) had an inner radius of 4.76 cm, outer radius of 5.08 cm, and length of 16.51 cm, while the planar target was a flat disk with a radius of 3.81 cm. In the hollow cathode configuration, the substrate was inserted into the volume of the hollow target (see supplementary material) and, as such, the sputtering working distance in both the planar and hollow cathode equaled the cylindrical target radius of 4.76 cm. Prior to sputtering coatings, the current-voltage or I-V characteristics of the sputtering discharge plasmas at the substrate surface were obtained using a cylindrical Langmuir probe (radius 0.254 mm) with a W wire tip (length 12.7 mm), using a similar probe construction as seen in the work done by Fang and Marcus [36]. Plasma measurements were taken at deposition power densities of 0.4 W cm^{-2}, 0.6 W cm^{-2}, 0.8 W cm^{-2}, 1.0 W cm^{-2}, and 1.2 W cm^{-2} with Ar pressures of 3, 6, 12, and 30 mTorr in the hollow cathode and Ar pressures of 3 and 6 mTorr in the planar cathode. Power density was defined as the applied sputtering power divided by the surface area of the sputtering target; the planar sputtering target had a surface area of 46 cm^2 and the hollow cathode had a surface area of 494 cm^2. The probe tip was positioned at the same working distances as the substrates with respect to the hollow and planar cathode target surfaces and was biased from −80V to 80V. The W filament probe tip was replaced before the coating thickness reached 2 microns, which was approximately 1% of the tip diameter, to prevent significant material build up from affecting probe accuracy. The measured I–V curves were graphically utilized to determine the ion saturation current, ion flux, and electron temperature. Ion densities, n_i, were calculated using the following equation, which is derived from the Bohm sheath theory. I_{is} is the saturation current, T_e is the electron temperature, A_{probe} is the known area of the probe tip, m_i is the ion mass, and k is Boltzman's constant [37–39].

Table 1. Summary of the hollow and planar cathode sputtering parameters and measured deposition conditions.

Sample	Power Density (W cm^{-2})	Argon Pressure (mTorr)	Sputtering Rate (nm s^{-1})	Homologous Temperature (T/T_m)	Ion Density (10^{12} cm^{-3})
HC 1	0.4	3.00	1.10	0.10	0.70 ± 0.21
HC 2	0.4	6.00	0.77	0.13	0.70 ± 0.30
HC 3	0.4	12.00	0.86	0.15	0.61 ± 0.01
HC 4	0.4	30.00	1.02	0.12	0.53 ± 0.14
PLNR 1	0.4	3.00	0.29	0.04	0.40 ± 0.01
PLNR 2	0.4	6.00	0.28	0.05	0.29 ± 0.03
HC 5	1.2	3.00	2.25	0.20	2.02 ± 0.34
HC 6	1.2	6.00	2.12	0.23	2.31 ± 0.55
HC 7	1.2	12.00	2.61	0.23	1.39 ± 0.22
HC 8	1.2	30.00	3.18	0.22	1.11 ± 0.11
PLNR 3	1.2	3.00	0.82	0.06	0.66 ± 0.04
PLNR 4	1.2	6.00	0.72	0.07	0.43 ± 0.04

$$n_i = \frac{I_{is}}{0.6 \cdot e \cdot A_{probe}\sqrt{\frac{k \cdot T_e}{m_i}}} \quad (1)$$

Following plasma characterization, 1 μm thick films were synthesized at the low and high power densities at each of the varying gas pressures. A summary of the synthesis conditions and local plasma properties for the deposited coatings can be seen in table 1. Film thickness was determined by the deposition rate multiplied by the total deposition time. To ensure consistent film thicknesses at the different sputtering parameters and target geometries, deposition time was adjusted so that each resulting film was 1 μm thick. The deposition rates were measured using an Ambios XP-2 profilometer and the homologous temperature (T/T_m) was measured using k-type thermocouples (Thermoelectric). The deposited films were characterized using XRD, SEM, and EBSD to study the film texturing, crystallinity, and surface morphology. A Rigaku Ultima-IV diffractometer was used to obtain XRD spectra with 2θ scans performed on the range of 30° to 110° at a rate of 1° min^{-1} and step size of 0.08° using Cu Kα radiation. The top surface and cross-sectional surface morphologies were imaged using a Nova NanoSEM 450 Field Emission SEM. Images were taken using the immersion lens at an accelerating voltage of 10kV and spot size of 4.0. From the SEM micrographs, the average feature sizes were obtained by averaging 200 measurements from each sample using Image-J software. EBSD was performed on film cross-sections using a Helios G4 PFIB UXe DualBeam FIB/SEM and data was analyzed using the Oxford Instruments Aztec Crystal software. The cross-sections were polished using the Xe ion beam and subsequently analyzed with EBSD at an accelerating voltage of 15kV and current of 3.2 nA to examine grain sizes and orientations. Average grain widths for each cross-section were determined by measuring 50 grains per sample using the Image-J software.

3. Results and discussion

3.1. Plasma analysis and film texturing

A fundamental understanding of the influence of target geometry on sputtered film microstructure and morphology should consider the plasma conditions, deposition pathways, and film growth mechanisms of sputtered particles. Therefore, Langmuir probe analysis was conducted to analyze the evolution of the plasma's ion density with respect to power density and pressure to investigate differences in ion production and bombardment for planer and ICM geometries. Figure 1 presents measured ion densities recorded over a range of sputtering power densities and pressures as well as corresponding XRD patterns taken at the low and high power densities (0.4 W cm^{-2} and 1.2 W cm^{-2}). Power density, which is the applied power divided by the surface area of the sputtering target, was chosen as a unifying parameter between the two configurations to normalize differences in target surface area. Figure 1(a) shows that the measured ion density is dependent on both power density and Ar pressure, increasing with applied power (as electron density and energy increases to more frequently ionize neutral gas atoms) and decreasing with increasing gas pressures (due to higher particle collision rates reducing electron energy and overall ionization). These observations agree with a previous study conducted by Metwaly and Elbashar that characterized a hollow cathode plasma and observed a decrease in electron temperature and ion density at higher gas pressures as well as an increase in ion density with increasing current densities [40]. Ion density has also been linked to pressure via Paschen's Law, which explains that the necessary potential to ionize a gas atom is directly proportional to the pressure and the spacing of electrodes; thus, a greater potential is needed to ionize gas at a higher pressure [41]. Over the measured range of power densities and Ar

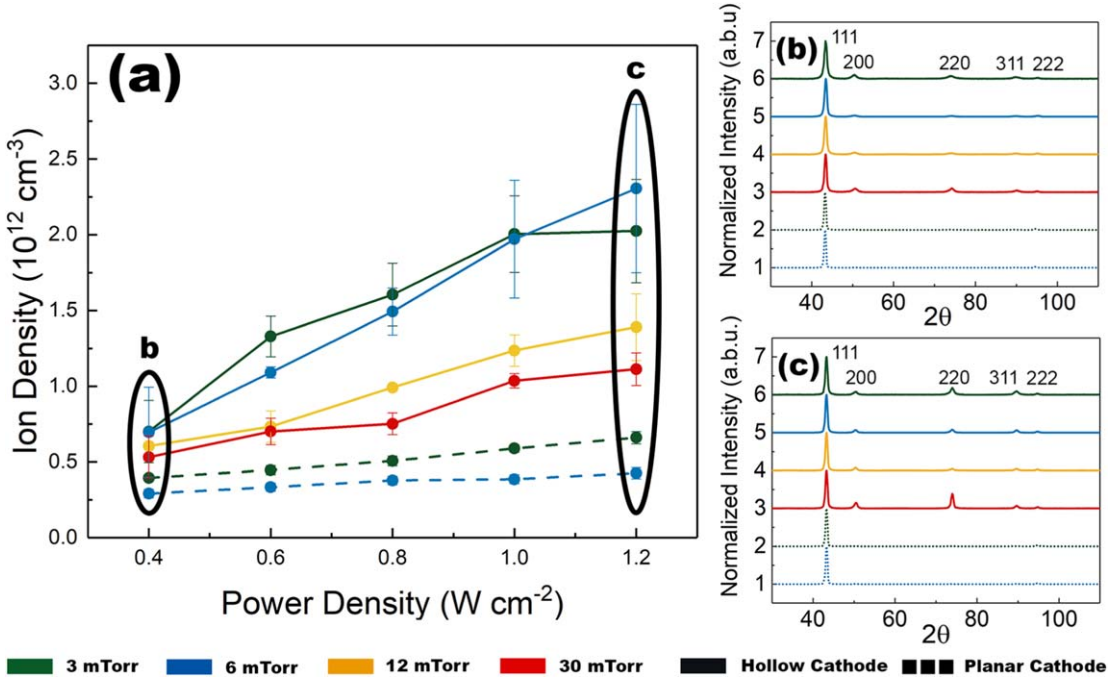

Figure 1. (a) Plotted Langmuir probe measured ion densities plots for hollow and planar cathode sputtering plasmas as a function of power density at varying Ar pressures. (b) x-rayX-ray diffraction (XRD) patterns for the films sputtered at the low power density (0.4 W cm^{-2}), which are indicated by the black oval on the left side of figure 1(a). (c) XRD patterns for the films sputtered at the high power density (1.2 W cm^{-2}), which are indicated by the black oval on the right side of figure 1(a). Hollow cathode samples and measurements are represented by a solid line, the planar cathode samples and measurements have a dashed line. Respective gas pressures are color coded and the main XRD intensity peaks are labeled.

pressures, the hollow cathode exhibited greater ion densities and a steeper ion density slope than the planar cathode, which indicates that ion density increases at a faster rate in the ICM; these differences are due to the changing cathode geometry extending electron mean free paths [17, 18].

Given the correlations between power density, argon pressure, and ion density identified by Langmuir probe measurements, samples were sputtered at each pressure at the low and high power densities, as indicated by the circled regions in figure 1(a), and analyzed using XRD to show changes in film texture. The corresponding XRD patterns for the planar and hollow cathode sputtered films are depicted in figure 1(b) (0.4 W cm^{-2}) and 1(c) (1.2 W cm^{-2}), where the sputtering pressures are represented by the color of the XRD patterns. At both power densities, the planar films have strong (111) texturing, while the ICM sputtered films display primarily a (111) texturing with additional peaks. Table 1 provides a summary of the sputtering parameters and plasma conditions for each film. From this table, it is seen at the same power density and pressure that hollow cathode sputtering yields greater deposition rates, homologous temperatures, and ion densities than the planar configuration. The presence of non (111) planes in the ICM sputtered samples is likely due to the wider range of angles of incidence and increased sputtering rates decreasing particle mobility and altering film growth directions during deposition, which can limit the formation of the lowest energy (111) planes. Additionally, it is seen in the hollow cathode samples that higher deposition rates in conjunction with lower ion densities may have further increased the random texturing, yielding greater amounts of higher energy (non (111)) planes. For example, in figure 1(c), the high-power density ICM sample sputtered at 30 mTorr had the largest (220) peak. Altogether, Langmuir probe analysis highlighted that transitioning from a planar to a hollow cathode target geometry alters the plasma ion density and the deposition environment during sputtering, while XRD showed changes in texture due to varying particle mobility during film growth.

3.2. Surface morphology characterization

Figures 2 and 3 link deposition conditions to film microstructure and morphology in the low and high-power density samples, respectively. The as-sputtered top surface morphologies and measured feature sizes for the hollow and planar cathode samples sputtered over the range of Ar pressures at the low power density (0.4 W cm^{-2}) are depicted in figure 2. Comparing films deposited by the two target geometries at the same Ar pressure (see figures 2(a) versus (e) and (b) versus (f)), the hollow cathode tends to yield more voided and porous top surface film morphology with significantly larger feature sizes. For the planar films, increasing the gas pressure from 3 to 6 mTorr did not significantly change film morphology, but did reduce feature size by decreasing the

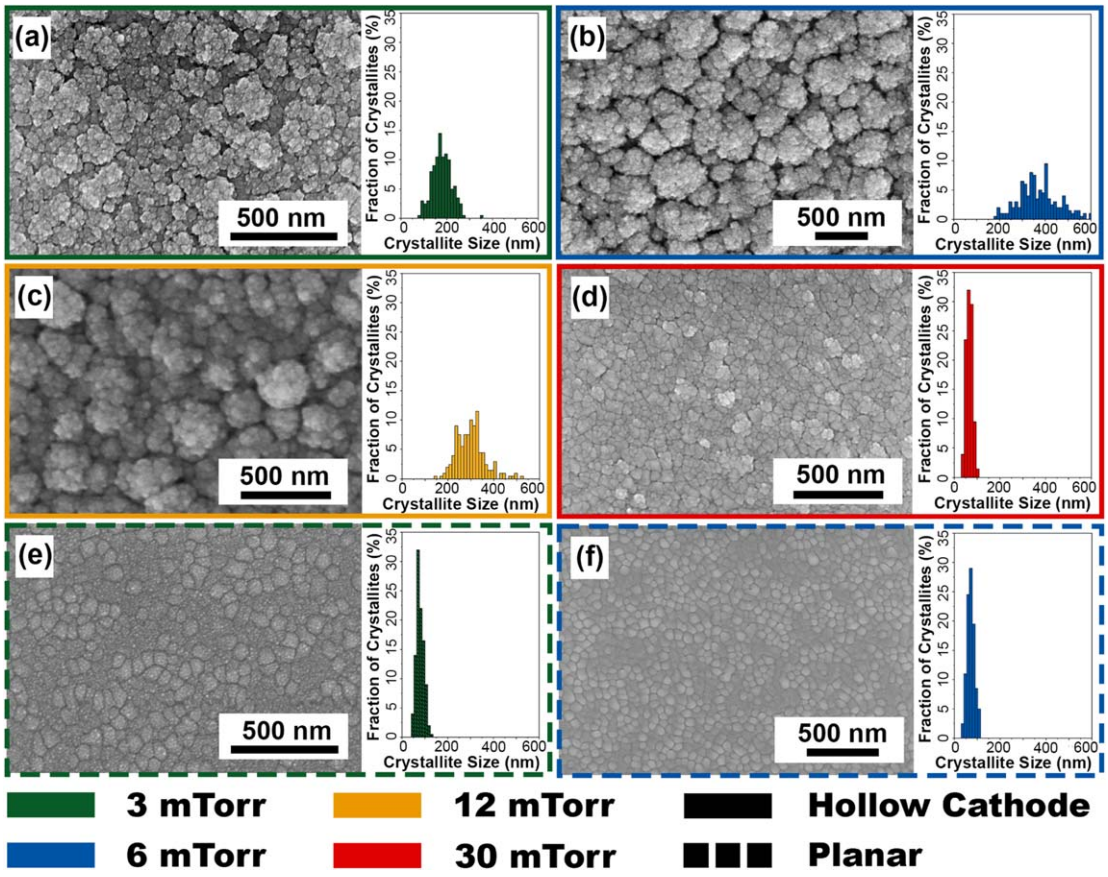

Figure 2. Scanning electron microscopy (SEM) micrographs of the as-deposited top surface morphologies at 0.4 W cm^{-2} power density for the hollow cathode (a)–(d) and planar cathode (e)–(f) films sputtered at gas pressures between 3 to 30 mTorr. The hollow cathode images have a solid border, the planar cathode images have a dashed border, and gas pressures are color coded. Feature sizes for each film are shown to the right of the corresponding SEM image.

energy of the deposited flux and thus overall adatom mobility. In the ICM sputtered films, changes in deposition parameters, such as Ar pressure, lead to greater variation in film morphology and feature size. Voids and porosity in hollow cathode films sputtered within the target volume has been reported in literature and can be attributed to higher deposition rates and a wider range of angles of incidence with the surface compared to the planar cathode [16, 18]. However, given the increased ion density in the ICM, it is apparent that additional factors influence the change in film morphology, which can be observed when comparing films deposited at different Ar pressures. For example, voids around crystallites, such as those present in figures 2(a)–(c), which were sputtered at 3, 6, and 12 mTorr respectively, originate from adatom mobility and film growth induced by ion bombardment. Island growth occurs as adatoms coalesce and this in turn leads to void formation due to adatom-depleted regions [42–44]. Figure 2(d) highlights the inverse of this relationship, forming smaller top surface features and adatom-depleted regions compared to figures 2(a)–(c), which can be attributed to the increase in Ar pressure to 30 mTorr limiting ion bombardment and adatom mobility by lowering the ion density.

Figure 3 presents the as-sputtered top surface morphologies and measured feature sizes for the hollow and planar cathode samples sputtered over the range of Ar pressures at the high power density (1.2 W cm^{-2}). Table 1 shows that the corresponding deposition rates more than doubled for both configurations and the ion density increased at a faster rate in the ICM than the planar cathode. Additionally, homologous temperature increased in the hollow cathode, but remained relatively constant for the planar geometry. The planar films (figures 3(e) and (f)) display a similar morphology to the low power density planar samples (figures 2(e) and (f)) with an increase in feature size that can be attributed to greater particle energy during deposition at the high power density. In contrast, a distinct change in morphology is observed when comparing the low and high power density ICM sputtered films (figures 2(a)–(d) and figures 3(a)–(d), respectively). At the high power density, greater deposition rates caused feature size to decrease compared to the low power density samples because of growing islands competing for surface area. Given the wide range of angles of incidence during ICM sputtering, it would be expected that higher deposition rates would also yield a more voided morphology; however, it was observed that the high power density films in figures 3(a)–(d) achieved a denser top surface morphology than the low power

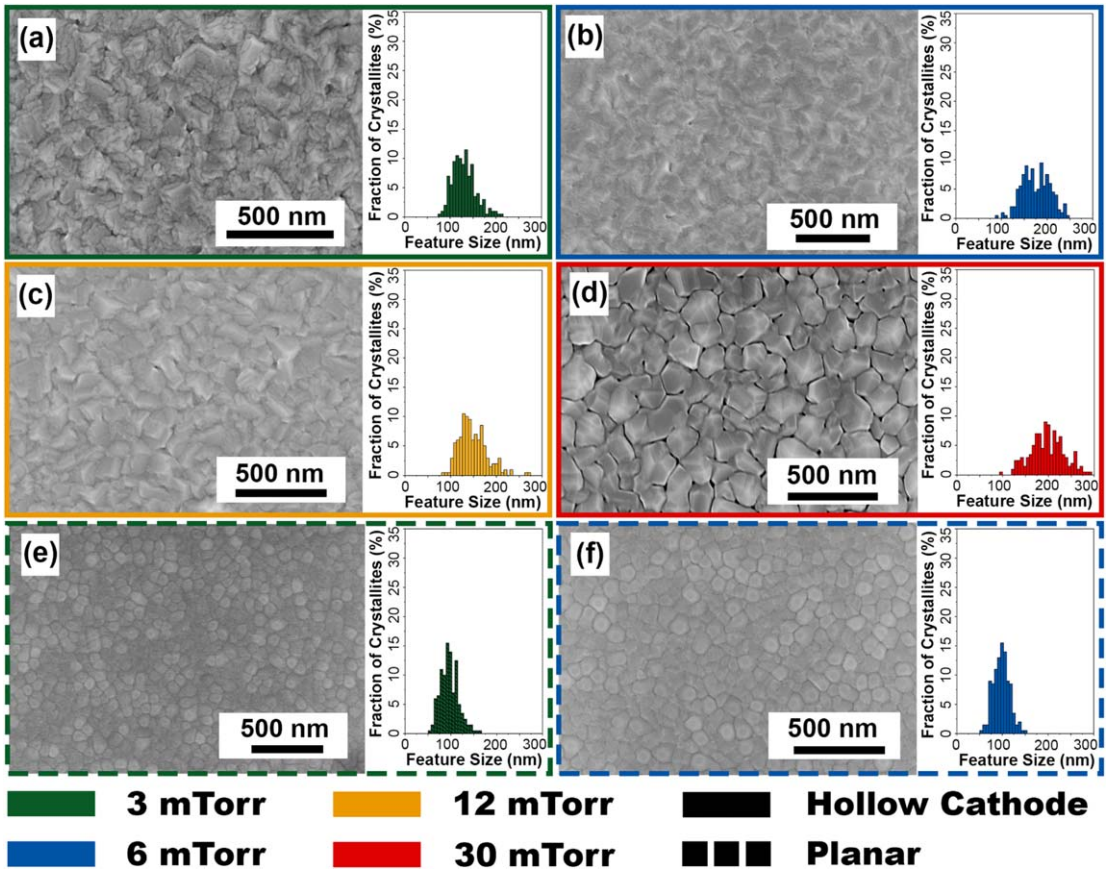

Figure 3. Scanning electron microscopy (SEM) micrographs of the as-deposited top surface morphologies at 1.2 W cm^{-2} power density for the hollow cathode (a)–(d) and planar cathode (e)–(f) films sputtered at gas pressures between 3 to 30 mTorr. The hollow cathode images have a solid border, the planar cathode images have a dashed border, and gas pressures are color coded. Feature sizes for each film are shown to the right of the corresponding SEM image.

density samples in figures 2(a)–(d). This is due to the greater homologous temperature and ion density increasing deposition energy and particle mobility during film formation. The samples sputtered at 3, 6, and 12 mTorr (figures 3(a)–(c)) highlight this change in film growth, as increased adatom mobility and surface diffusion allow the films to achieve denser top surface morphologies by preventing the formation of adatom depleted zones. It should be noted that unlike the 3, 6, and 12 mTorr samples, the film sputtered at 30 mTorr (figure 3(d)) shows residual voids on the top surface due to the greater sputtering pressure limiting densification by reducing ion bombardment and adatom mobility. In general, as power density increases over this range, the dominant growth mechanisms in the planar cathode remain constant, while, due to its target geometry, ICM sputtering transitions from adatom mobility and diffusion limited film growth to growth with enough particle mobility to enable the formation of denser coating morphologies. This demonstrates that the hollow cathode has competing factors influencing film formation including higher deposition rates, wider range of angles of incidence, growing homologous temperatures, and greater change in ion density.

3.3. Orientation, grain size, and global morphology

From the previous section, distinct relationships between target geometry and coating morphology were established, which can be further evaluated by studying the film's microstructure. Figure 4 presents EBSD grain orientation maps for hollow cathode (4a, 4b, and 4e) and planar cathode (4c,4d) films sputtered at both the low (0.4 W cm^{-2}) and high power (1.2 W cm^{-2}) densities as a function of ion density, where increasing ion density is denoted by the arrow. The hollow cathode cross-sections in figures 4(a), (b), and (e) revealed a columnar microstructure, grain widths of roughly 70–80 nm, and a wide range of grain orientations. Similar columnar microstructures and grain sizes were observed in the planar cathode samples in figures 4(c) and (d); however, the planar samples displayed a higher degree of (111) grain orientations. The vertical column (figures 4(a)–(c)) is used to compare the cross-sectional microstructures of samples sputtered at the same power density (1.2 W cm^{-2}) with increasing ion density and homologous temperature, while the horizontal row (figures 4(c)–(e)) is used to compare cross-sectional microstructure for samples sputtered at similar ion densities at the low and high power densities. Although changes in target geometry and sputtering conditions led to over a threefold increase

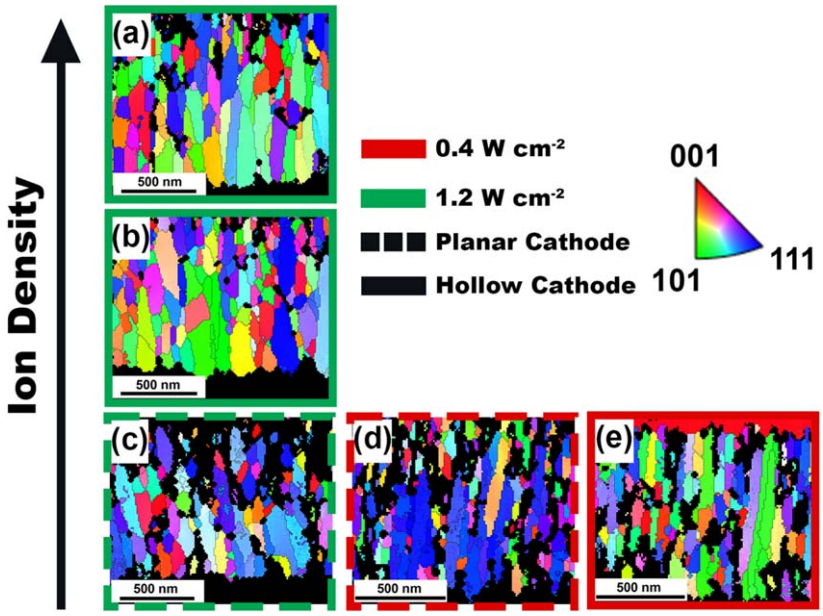

Figure 4. Electron backscatter diffraction (EBSD) grain orientation maps for planar (dashed border) and hollow cathode (solid borders) sputtered films. The vertical column (a)–(c) shows samples sputtered at the same power density (1.2 W cm^{-2}, green border) with increasing ion densities. The horizontal row (c)–(e) displays samples sputtered with similar ion densities at both the low (0.4 W cm^{-2}, gray border) and high (1.2 W cm^{-2}) power densities. The inverse pole figure (IPF) triangle defining grain orientations is to the right of the EBSD scans.

in ion density, homologous temperature, and deposition rate, all grain orientation maps revealed similar Zone T microstructures and grain sizes for all samples. This could be due to limited change in bulk diffusion over the range of particle energies and homologous temperatures observed in this study, which in turn would prevent the formation of Zone 2/3 microstructures as shown in the Anders structure zone map predictions [12]. Additionally, for the samples with higher ion density, the effects of increased energy from ion bombardment could be limited by the greater deposition rates as the adatoms lose energy when colliding with newly sputtered particles. This is supported by previous works, which have shown that the ion-to-neutral atom ratios can affect microstructure, texturing, and morphology [6, 45]. However, regardless of changes in bulk diffusion, a columnar structure similar to planar sputtered films was not predicted for the ICM sputtered samples due to the ICM's wide range of angles of incidence, as previous work has shown that altering the deposition angle during unidirectional PVD can change the film growth direction [6]. The observed columnar microstructure potentially indicates that target geometries that deposit material equally from all directions with respect to the substrate, such as the hollow cathode, can achieve similar microstructures to perpendicular unidirectional deposition. Thus, target geometry could alter top surface morphology by varying adatom mobility without changing bulk diffusion and the resulting film microstructure.

To highlight the differences in the evolution of hollow cathode film morphology as compared to the planar geometry, a graphical summary of the top surface (red border) and cross-sectional (blue border) morphologies as a function of ion density and homologous temperature is shown in figure 5. The planar film highlighted in the expanded circle in figure 5 demonstrates that unidirectional deposition can achieve a dense fully formed top surface layer even at low homologous temperatures and ion densities. This is possible as film coarsening can still occur at low fluxes and limited angular distributions during deposition. In contrast, due to the more complex target geometry, the hollow cathode sputtered films show a wide range of top surface and cross-sectional morphologies that are clearly influenced by the sputtering plasma and deposition environment. The change in target geometry causes a competition between the increased angles of incidence, homologous temperature, and ion bombardment on the particle mobility during film growth. An increase in either homologous temperature or ion density results in film densification and a less voided top surface morphology, as diffusion and adatom mobility increase. Thus, in addition to traditional relationships observed in planar magnetron sputtering that can be used to alter film properties like grain size and texturing, more complex target geometries, like the hollow cathode, can also be used to influence film morphology by altering ion bombardment and angle of incidence during deposition. Although the plasma properties within the hollow cathode are linked to its deposition parameters, which prevent arbitrarily varying ion and electron densities like other I-PVD techniques, sputtering within the hollow cathode volume can begin to bridge traditional and ion-assisted sputtering to further manipulate coating morphology and microstructure.

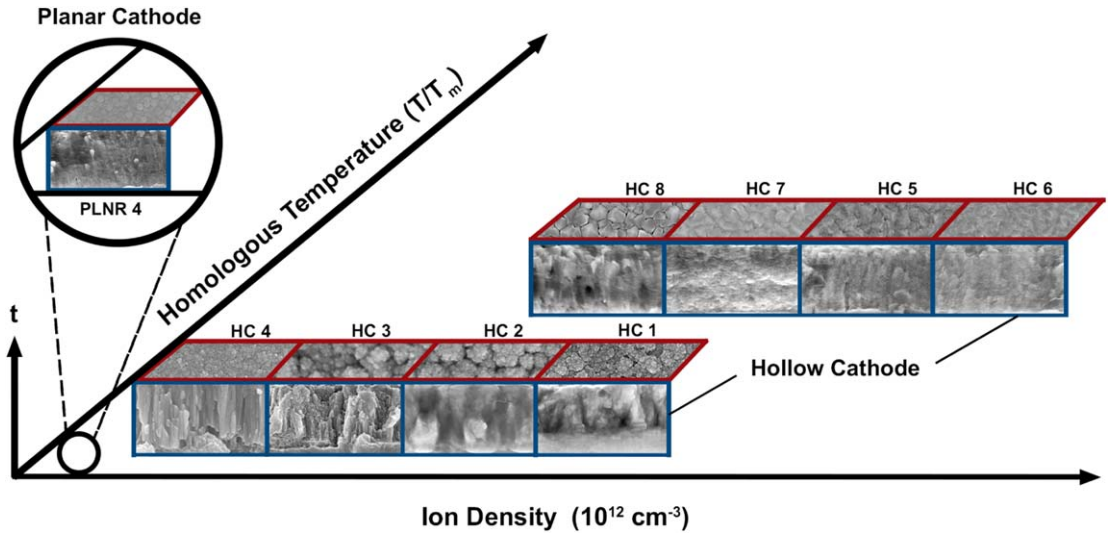

Figure 5. Graphical summary of planar and hollow cathode top-surface and cross-sectional morphologies with respect to ion density (x-axis) and homologous temperature (T/T_m) (y-axis), where coating thickness is shown in the z-axis. The as-sputtered top surface morphologies are outlined in red and the cross-sectional morphologies are outlined in blue; all boxes are roughly 1.5 micron in length. Sample labels correspond to table 1.

4. Conclusion

Sputtering target geometry was linked to plasma characteristics and coating morphology in order to provide a fundamental understanding of the impact of cathode shape on film growth. Langmuir probe analysis of the sputtering plasmas revealed that the hollow cathode yields greater ion densities than the planar configuration at the same deposition conditions. For both target geometries, ion density decreased at higher gas pressures and increased at higher power densities. In addition, it was shown that ion density changes at a greater rate with respect to power density in the hollow cathode. For films synthesized at 0.4 W cm^{-2} and 1.2 W cm^{-2}, it can be seen that ICM sputtered samples have larger feature sizes and greater fluctuation in film morphology and microstructure with respect to the deposition conditions. This is caused by competing factors influencing growth that are not apparent in planar deposition, such as different angles of incidence, increased deposition rates, larger variation in homologous temperatures, and greater ion bombardment. Due to changes in temperature, particle energy, and ion density, it is observed that films sputtered inside the hollow cathode volume can transition from voided to dense top surface morphologies as increased particle mobility aids uniform film growth and prevents adatom depleted regions. Interestingly, cross-sectional EBSD characterization revealed that target geometry can alter the top surface morphology but changes in microstructure and grain size were limited. Overall, this study offers insight into the global impact of target geometry on film growth in order to expand morphological and microstructural regimes, which can be used to guide sputtering with non-planar systems, like the hollow cathode.

Acknowledgments

This work was supported by the National Science Foundation (Grant Number OISE-2106597). Adie Alwen acknowledges fellowship support through the National Defense Science and Engineering Graduate (NDSEG) Fellowship Program, which is offered by the Department of Defense and sponsored by the Air Force Research Laboratory, the Office of Naval Research, and the Army Research Office. The authors would also like to acknowledge the Core Center of Excellence in Nano Imaging (CNI) at the University of Southern California for the characterization facilities.

Data availability statement

The data that support the findings of this study are available upon reasonable request from the authors.

Declaration of competing interest

The authors declare that they have no competing financial interests or personal relationships that could have appeared to influence the work reported in this paper.

CRediT author contribution statement

Adie Alwen: Investigation, Conceptualization, Methodology, Formal Analysis, Visualization, Writing—Original Draft, Writing—Review & Editing. Andrea Hodge: Writing—Review and Editing, Supervision, Project Administration, Validation, Funding Acquisition.

ORCID iDs

Adie Alwen https://orcid.org/0000-0002-4967-3041
Andrea M Hodge https://orcid.org/0000-0001-9945-7841

References

[1] Thornton J 1986 The microstructure of sputter-deposited coatings *J. Vac. Sci. Technol. A* **4** 3059–65
[2] Gudmundsson J T 2020 Physics and technology of magnetron sputtering discharges *Plasma Sources Sci T.* **29** 113001
[3] Kelly P J and Arnell R D 2000 Magnetron sputtering: a review of recent developments and applications *Vacuum* **56** 159–72
[4] Kana J K *et al* 2010 Thermochromic nanocrystalline Au–VO2 composite thin films prepared by radiofrequency inverted cylindrical magnetron sputtering *Thin Solid Films* **518** 1641–7
[5] Manova D, Gerlach J W and Mändl S 2010 Thin film deposition using energetic ions *Materials.* **3** 4109–41
[6] Greczynski G, Jensen J and Hultman L 2011 Mitigating the geometrical limitations of conventional sputtering by controlling the ion-to-neutral ratio during high power pulsed magnetron sputtering *Thin Solid Films* **519** 6354–61
[7] Rossnagel S and Cuomo J 1989 Film modification by low energy ion bombardment during deposition *Thin Solid Films* **171** 143–56
[8] Harper J M, Cuomo J J, Gambino R J and Kaufman H R 1985 Modification of thin film properties by ion bombardment during deposition *Nucl Instrum Meth B.* **7** 886–92
[9] Mbam S O, Nwonu S E, Orelaja O A, Nwigwe U S and Gou X-F 2019 Thin-film coating; historical evolution, conventional deposition technologies, stress-state micro/nano-level measurement/models and prospects projection: a critical review *Mater. Res. Express* **6** 122001
[10] Rossnagel S M 2020 Magnetron sputtering *J. Vac. Sci. Technol. A* **38** 060805
[11] Motegi N *et al* 1995 Long-throw low-pressure sputtering technology for very large-scale integrated devices *J. Vac. Sci. Technol. B* **13** 1906–9
[12] Anders A 2010 A structure zone diagram including plasma-based deposition and ion etching *Thin Solid Films* **518** 4087–90
[13] Patel N P and Chauhan K V 2022 Effect of sputtering power and substrate temperature on structural, optical, wettability and anti-icing characteristics of aluminium doped zinc oxide *Mater. Res. Express* **9** 076402
[14] Solis-Pomar F, Cruz A F, Menchaca J, Meléndrez M and Pérez-Tijerina E 2018 Study of the structural properties of nanostructured PbS thin films deposited by RF sputtering at room temperature *Mater. Res. Express* **5** 106403
[15] Thornton J 1974 Influence of apparatus geometry and deposition conditions on the structure and topography of thick sputtered coatings *J. Vac. Sci. Technol. A* **11** 666–70
[16] Thornton J and Hedgcoth V 1974 Tubular hollow cathode sputtering onto substrates of complex shape *J. Vac. Sci. Technol. A* **12** 93–7
[17] Muhl S and Perez H 2015 The use of hollow cathodes in deposition processes: a critical review *Thin Solid Films* **579** 174–98
[18] Rane R, Joshi A, Akkireddy S and Mukherjee S 2019 Comparative study of discharge characteristics and associated film growth for post-cathode and inverted cylindrical magnetron sputtering *Pramana - J Phys.* **92** 1–9
[19] Glocker D, Romach M, Scherer G, Eichenberger J and Lanzafame J 2014 Inverted cylindrical magnetron sputtering: advantages of off-axis alignment of substrates on the deposition of optical coatings *Vak. Forsch. Prax.* **26** 18–23
[20] Klawuhn E, D'couto G, Ashtiani K, Rymer P, Biberger M and Levy K 2000 Ionized physical-vapor deposition using a hollow-cathode magnetron source for advanced metallization *J. Vac. Sci. Technol. A* **18** 1546–9
[21] Koch H, Friedrich L, Hinkel V, Ludwig F, Politt B and Schurig T 1991 Hollow cathode discharge sputtering device for uniform large area thin film deposition *J. Vac. Sci. Technol. A* **9** 2374–7
[22] Poluektov N, Tsar'gorodsev Y P, Usatov I, Evstigneev A and Kamyschov I 2015 Plasma parameters of the hollow cathode magnetron inside and downstream *Plasma Sources Sci T.* **24** 035009
[23] Glocker D A, Romach M M and Lindberg V W 2001 Recent developments in inverted cylindrical magnetron sputtering *Surf Coat Tech.* **146** 457–62
[24] Abe S, Takahashi K, Mukaigawa S and Takaki K 2020 Comparison of plasma characteristics of high-power pulsed sputtering glow discharge and hollow-cathode discharge *Jpn J of Appl Phys.* **60** 015501
[25] Esparza-Contro C *et al* 2020 Microstructures of titanium oxide thin films grown continuously on stainless steel wires by PVD in an inverted cylindrical magnetron: Towards an industrial process *Surf Coat Tech.* **389** 125643
[26] Todoran A, Mantel M, Bes A, Vachey C and Lacoste A 2014 Control of particle flux and energy on substrate in an inverted cylindrical magnetron for plasma PVD *Plasma Sources Sci T.* **23** 065039
[27] Kaneko T and Nittono O 1997 Improved design of inverted magnetrons used for deposition of thin films on wires *Surf Coat Tech.* **90** 268
[28] Garcia-Taormina A R, Kurpiers C M, Schwaiger R and Hodge A M 2021 Coatings for core-shell composite micro-lattice structures: varying sputtering parameters *Adv. Eng. Mater.* **24** 2101264
[29] Eberhardt M G, Hodge A M and Branicio P S 2022 Atomistic modeling of physical vapor deposition on complex topology substrates *Comput. Mater. Sci.* **203** 111111

[30] Garcia-Taormina A R, Alwen A, Schwaiger R and Hodge A M 2021 A review of coated nano-and micro-lattice materials *J. Mater. Res.* **36** 3607–27
[31] Montemayor L and Greer J 2015 Mechanical response of hollow metallic nanolattices: combining structural and material size effects *J. Appl. Mech.* **82** 7
[32] Juarez T, Schroer A, Schwaiger R and Hodge A M 2018 Evaluating sputter deposited metal coatings on 3D printed polymer micro-truss structures *Mater Design.* **140** 442–50
[33] Gao L *et al* 2018 High-entropy alloy (HEA)-coated nanolattice structures and their mechanical properties *Adv. Eng. Mater.* **20** 1700625
[34] Zhang X *et al* 2018 Three-dimensional high-entropy alloy–polymer composite nanolattices that overcome the strength–recoverability trade-off *Nano Lett.* **18** 4247–56
[35] Velasco L, Polyakov M N and Hodge A M 2014 Influence of stacking fault energy on twin spacing of Cu and Cu–Al alloys *Scripta Mater.* **83** 33–6
[36] Fang D and Marcus R K 1990 Use of a cylindrical Langmuir probe for the characterization of charged particle populations in a planar, diode glow discharge device *Spectrochim. Acta B* **45** 1053–74
[37] Merlino R L 2007 Understanding Langmuir probe current-voltage characteristics *Am. J. Phys.* **75** 1078
[38] Cherrington B 1982 The use of electrostatic probes for plasma diagnostics—a review *Plasma Chem Plasma P.* **2** 113–40
[39] Navid A and Hodge A 2012 Nanostructured alpha and beta tantalum formation—Relationship between plasma parameters and microstructure *Mater. Sci. Eng. A* **536** 49–56
[40] Metwaly K H and Elbashar Y H 2022 Probe measurements of a plasma hollow cathode discharge used as a sputter source for copper thin film *J Opt-Uk.* **51** 241–5
[41] Keidar M and Beilis I 2013 *Plasma Engineering: Applications from Aerospace to Bio and Nanotechnology* (Cambridge, Massachusettes: Academic Press)
[42] Marinov M 1977 Effect of ion bombardment on the initial stages of thin film growth *Thin Solid Films* **46** 267–74
[43] Michely T and Comsa G 1991 Generation and nucleation of adatoms during ion bombardment of Pt (111) *Phys. Rev. B* **44** 8411–4
[44] Petrov I, Barna P, Hultman L and Greene J 2003 Microstructural evolution during film growth *J. Vac. Sci. Technol. A* **21** S117–28
[45] Ensinger W 1997 Low energy ion assist during deposition—an effective tool for controlling thin film microstructure *Nucl Instrum Meth B.* **127** 796–808